Electrochimica Acta 147 (2014) 470–482

Contents lists available at ScienceDirect

Electrochimica Acta

journal homepage: www.elsevier.com/locate/electacta

Optimal Regularization in Distribution of Relaxation Times applied to Electrochemical Impedance Spectroscopy: Ridge and Lasso Regression Methods - A Theoretical and Experimental Study

Mattia Saccoccio[a], Ting Hei Wan[a], Chi Chen[a], Francesco Ciucci[a,b,*]

[a] Department of Mechanical and Aerospace Engineering, The Hong Kong University of Science and Technology, Kowloon, Hong Kong
[b] Department of Chemical and Biomolecular Engineering, The Hong Kong University of Science and Technology, Kowloon, Hong Kong

ARTICLE INFO

Article history:
Received 6 June 2014
Received in revised form
13 September 2014
Accepted 16 September 2014
Available online 28 September 2014

Keywords:
Electrochemical Impedance Spectroscopy
Distribution of Relaxation Times
Lasso Regularization
Ridge Regularization
Solid Oxide Fuel Cells
Lithium-ion Batteries

ABSTRACT

The Distribution of Relaxation Times (DRT) is an approach of particular interest to the interpretation of Electrochemical Impedance Spectroscopy (EIS) measurements. The DRT allows direct access to the time characteristics of the electrochemical system under study. Obtaining the DRT from noisy EIS data requires solving an ill-posed problem using regularization methods. In this work we investigate the optimal choice of the regularization parameter in the case of ridge regression. For this purpose we propose two novel sets of test functions known as real and imaginary discrepancy test function, and real and imaginary cross-validation test functions. Furthermore, we show the validity of these tests with synthetic and real experiments. By applying the optimal regularization parameters, the DRT results from the synthetic experiments (an RC circuit, a ZARC, and a fractal element) successfully reproduce the known exact DRT. Additionally, in the cases taken from electrochemical practice (a collection of RC circuits, a symmetric cell, and a commercial Li-ion battery) our approach confirms the ability to identify various timescales. Additionally, we study the output of the regularization using Least Absolute Shrinkage and Selection Operator (Lasso) and we highlight the added value given by the synergetic use of Lasso and ridge regression.

1. Introduction

Complex systems characterized by multiple timescales can be found in many electrochemical applications such as fuel cells, batteries, and chemical sensors. Similarly, these systems are reported in biological and biomedical studies. The relaxation of such systems cannot be described by one rate constant only, instead a distribution of relaxation times is necessary. The latter, however, cannot be observed directly; yet it can be obtained from the spectrum of measured responses of the system to a series of perturbations at different frequencies. EIS [1] has established itself as the tool of choice for time-resolved electrochemical characterization. It is often possible to map the EIS spectrum to physically relevant phenomena, and this is particularly useful because it allows insights on the physics of transport phenomena and on the kinetics of reactions [2–8]. In particular, many significant quantities can be estimated, among others diffusion coefficients, reaction rates, charge-carrier concentrations, and dissociation and recombination parameter [9–12].

EIS is an experimental technique which provides valuable frequency information, bridging disparate timescales [13–15]. However, the interpretation of EIS experimental data can be challenging [3]. The most widely used method to analyze impedance data consists of constructing equivalent circuits that model the EIS response and closely fit the experimental data. However, this approach is known to have several limitations. For example, different configurations of equivalent circuits can provide nearly identical responses [16,17]. This adds further burden to the necessary *a priori* circuit choice, which in turn impacts the physico-chemical interpretation of the EIS data. An other proposed approach to interpret EIS data is the differential impedance analysis [18]. This method also allows the identification of the time constants of the system under study, and has been applied, for example, to solid state materials [19], solid oxide fuel cells [20], and Li-ion batteries [21,22]

The DRT is an alternative way to analyze EIS data [23,24]. Compared to other methods, the DRT representation isolates the processes with different time constants, and it gives direct access to the distribution of the timescales of the system under study, i.e., to the relaxation times. Moreover, an approach based on the

* Corresponding author.
E-mail addresses: mefrank@ust.hk, francesco.ciucci@gmail.com (F. Ciucci).

http://dx.doi.org/10.1016/j.electacta.2014.09.058
0013-4686/

Nomenclature

$\gamma(\tau)$	Distribution function of relaxation times
$\delta(\tau)$	Dirac distribution centered at 0
λ	Regularization parameter
$\phi_n(\tau)$	Discretization basis
τ	Relaxation time
τ_0	Characteristic time constant of the model
$\mathbf{A}$	Approximation matrix for the DRT
C	Capacitance of the capacitor in the RC circuit
$e_\gamma(\ln\tau)$	Discretization error for the DRT
$e_{Z(f)}$	Discretization error for the impedance spectrum
E	Error between resulted and exact DRT
f	Frequency
$g(\tau)$	Distribution function
K	Kernel function of the Fredholm integral
$\mathbf{L}$	First derivative differentiation matrix
$P(\mathbf{x})$	Regularization penalty
R_∞	Resistance at infinite frequency
R_0	Resistance at zero frequency
R_{ct}	Charge transfer resistance
R	Resistance of the resistor in the RC circuit
x_n	Weight applied to each basis function
$\mathbf{x}$	Vector of the weights applied to each basis function
w_n	Weighting function for the complex nonlinear least-squares fitting
Z_{model}	Modeled impedance
Z'_{model}	Real part of the modeled impedance
Z''_{model}	Imaginary part of the modeled impedance
Z_{exp}	Experimental impedance
Z'_{exp}	Real part of the experimental impedance
Z''_{exp}	Imaginary part of the experimental impedance
$\mathbf{Z}$	Complex impedance vector
$\mathbf{Z}'$	Real part of the impedance vector
$\mathbf{Z}''$	Imaginary part of the impedance vector
$\mathbb{S}$	Sum of squares in the complex nonlinear least-square fitting

DRT overcomes some of the issues previously mentioned as, for example, it does not require equivalent circuit fitting.

The DRT can be obtained by fitting the experimental data against the response of a series of Voigt elements [25–27], as shown in Fig. 1. Such a general circuit gives a distribution of time constants. A number of groups have worked on this concept and have further generalized the Voigt-circuit approach [28,29]. It is currently understood that the DRT is related to the EIS data via a Fredholm integral equation of the first kind [30]. The Fredholm integral may be written in the general form:

$$u(r) = \int_a^b K(r,s)\nu(s)ds \tag{1}$$

where $\nu(s)$ is the real-valued function, which in our case describes the distribution of time constants, $K(r, s)$ is the kernel, and $u(r)$ is the experimental data, which in this work represents the experimentally measured impedance function, and where a and b are the integration limits. Thus, the problem is to obtain $\nu(s)$ with known $K(r, s)$ and $u(r)$. It is important to note that the inputs of the DRT, roughly corresponding to the $u(r)$, are noisy [31] because they are experimental data.

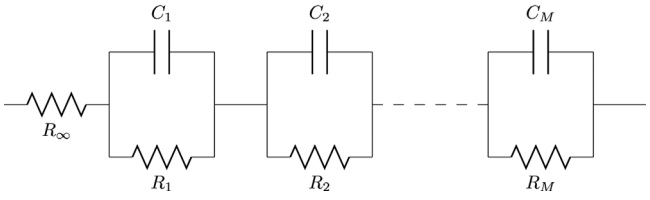

Fig. 1. Schematic representation of a Voigt circuit.

In addition, due to the large number of unknowns, the DRT problem is intrinsically ill-posed, meaning that the solution may not be unique, or it may be strongly unstable depending on experimental errors or even numerical truncation errors. Therefore, experimental data need to be processed in an *ad-hoc* manner in order to obtain a suitable DRT. Numerous methods to analyze the EIS via DRT have appeared in the literature, including ridge (or Tikhonov) regularization [31–35], preconditioned ridge regularization [36], Fourier filtering and subsequent fitting [37], Monte Carlo methods [3,38,39], maximum entropy methods [40], and genetic programming [28,41,42].

In this work, we focus on regularization of the DRT using ridge regression [43] and Lasso regression [44]. Regularization is a general method to solve an ill-posed problem, or prevent overfitting, by incorporating additional information to the problem under consideration. In regularized regression, noisy data is smoothed by adding an extra term to the usual least square regression. Regularized least square fitting requires the minimization of the following equation

$$\sum_{n=1}^{N}[y_n - h(x_1, x_2, \ldots x_N, f_n)]^2 + \lambda P(x_1, \ldots, x_N) \tag{2}$$

for N data points (y_n) taken at f_n and a fitting function $h(x_1, x_2, \ldots x_N, f_n)$. The penalization term $P(x_1, \ldots, x_N)$ is weighted using the regularization parameter $\lambda \geq 0$.

Ridge regularization has been widely applied to DRT, however, it is still unclear how much smoothing should be given to the data. In other words, how should the tuning parameter λ be chosen? In this work, we address this very issue using both simulated and real experiments. To do so, we develop two methods for parameter selection. These methods leverage on the minimization of a real and imaginary discrepancy test function, and on the minimization of real and imaginary cross-validation test functions respectively. In addition, we provide complementary results obtained using Lasso. Finally, we highlight the usefulness of careful parameter selection and of the Lasso.

2. Theory

2.1. Problem setting

The DRT analysis starts by modeling the experimental impedance response $Z_{\text{model}}(f)$ as the sum of a non-negative number R_∞ and an integral expression, namely

$$Z_{\text{model}}(f) = R_\infty + \int_0^\infty \frac{g(\tau)}{1 + i2\pi f\tau}\ \mathrm{d}\tau \tag{3}$$

where $g(\tau)$ represents the unknown non-negative distribution function and $K(f, \tau) = (1 + i2\pi f\tau)^{-1}$ is the kernel, a complex-valued function. Physically, this corresponds to stating that the impedance response is an infinite set of small parallel resistor-capacitor circuits placed in series. Typically, the use of (3) is impractical since the EIS data are usually taken and displayed in a logarithmic scale. We define instead a function $\gamma(\ln\tau) = \tau g(\tau)$ in order to write[1]

[1] We note that this is a bit of an abuse of notation: a more precise notation would require one to define $y = \ln\tau$ to set $Z_{\text{model}}(f) = R_\infty + \int_{-\infty}^{\infty} \frac{\gamma(y)}{1+i2\pi f\tau}\,\mathrm{d}y$, thus after

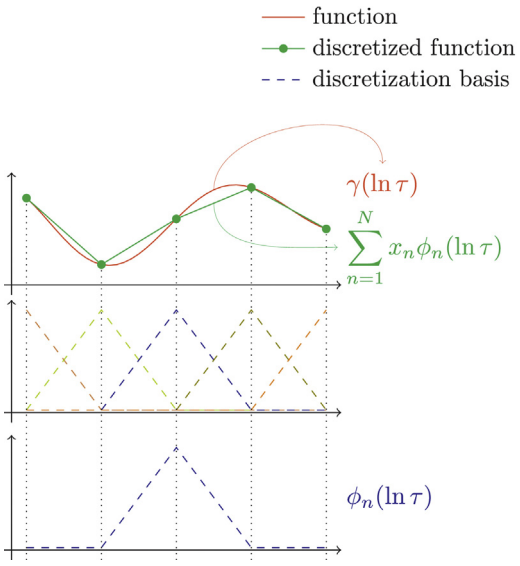

Fig. 2. The DRT γ (in red) and its piece-wise linear approximation (in green) are depicted in the upper panel. The latter is a linear combination of the basis functions ϕ_n plotted as dashed lines in the middle panel. Each basis is a tent function, as shown in the lower panel (blue dashed line).

$$Z_{\text{model}}(f) = R_\infty + \int_{-\infty}^{\infty} \frac{1}{1+(2\pi f\tau)^2}\gamma(\ln\tau)\ \ \mathrm{d}\ln\tau - i\int_{-\infty}^{\infty} \frac{2\pi f\tau}{1+(2\pi f\tau)^2}\gamma(\ln\tau)\ \ \mathrm{d}\ln\tau \tag{4}$$

The numerical treatment of (4) rests upon a suitable approximation of the function that needs to be obtained. Here, we approximate $\gamma(\ln\tau)$ on a piece-wise linear function, thus we choose a finite discretization basis $V = \{\phi_1(\ln\tau), \phi_2(\ln\tau), \ldots, \phi_N(\ln\tau)\}$ as illustrated in Fig. 2, and we write

$$\gamma(\ln\tau) = \sum_{n=1}^{N} x_n\phi_n(\ln\tau) + e_\gamma(\ln\tau) \tag{5}$$

where x_n are unknown positive numbers and $e_\gamma(\ln\tau)$ is the discretization error [45,46]. The condition that $x_n \geq 0$ is dictated by the constraint that each time process is actually a relaxation (a decaying exponential). In our case the N collocation points are the same as the measurement points.

It is important to note that the basis can be composed by Voigt elements[2] [15] as well as by other functions such as wavelets [47]. If we plug the expression (5) into (4), we obtain

$$Z_{\text{model}}(\mathbf{x}, f) = R_\infty + \sum_{n=1}^{N}\left[x_n\left(\int_{-\infty}^{\infty}\frac{1}{1+(2\pi f\tau)^2}\phi_n(\ln\tau)\ \ \mathrm{d}\ln\tau\right)\right] - i\sum_{n=1}^{N}\left[x_n\left(\int_{-\infty}^{\infty}\frac{2\pi f\tau}{1+(2\pi f\tau)^2}\phi_n(\ln\tau)\ \ \mathrm{d}\ln\tau\right)\right] + e_Z(f) \tag{6}$$

where $e_Z(f)$ is the discretization error [36,45,46]. The estimation of the variables x_n's is typically done by fitting the model expression (6) against experimental data. This implies that we seek to minimize the following kind of sum of squares[3]

$$\mathbb{S}(\mathbf{x}) = \sum_{n=1}^{N}\left[\frac{1}{w'_n}\left(Z'_{\text{exp}}(f_n) - Z'_{\text{model}}(\mathbf{x}, f_n)\right)^2 + \frac{1}{w''_n}\left(Z''_{\text{exp}}(f_n) - Z''_{\text{model}}(\mathbf{x}, f_n)\right)^2\right] \tag{7}$$

where $Z_{\text{exp}}(f)$ is 'N is the total number of frequencies f_n at which the impedance is measured. Furthermore, as we show in Appendix A, (7) can be rewritten in matrix notation as

$$\mathbb{S}(\mathbf{x}) = \left\|\boldsymbol{\Omega}'\left(\mathbf{Z}'_{\text{exp}} - \mathbf{A}'\mathbf{x}\right)\right\|_2^2 + \left\|\boldsymbol{\Omega}''\left(\mathbf{Z}''_{\text{exp}} - \mathbf{A}''\mathbf{x}\right)\right\|_2^2 \tag{8}$$

where $\mathbf{A}'$ and $\mathbf{A}''$ are suitable matrices obtained from (6). $\mathbf{Z}'$, $\mathbf{Z}''$, and $\mathbf{x}$ are N-dimensional vectors defined as $\left(\mathbf{Z}'\right)_n = Z'_{\text{exp}}(f_n)$, $\left(\mathbf{Z}''\right)_n = Z''_{\text{exp}}(f_n)$, and $(\mathbf{x})_n = x_n$ respectively. As mentioned in the introduction, the problem of minimizing $\mathbb{S}(\mathbf{x})$ is ill-posed, in that it gives highly oscillating solutions strongly dependent on the level of noise of the data and on the number of frequency measurements. Therefore, regularization methods may be employed, thereby solving a modified version of (8)

$$\mathbb{S}(\mathbf{x}) = \left\|\boldsymbol{\Omega}'\left(\mathbf{Z}'_{\text{exp}} - \mathbf{A}'\mathbf{x}\right)\right\|_2^2 + \left\|\boldsymbol{\Omega}''\left(\mathbf{Z}''_{\text{exp}} - \mathbf{A}''\mathbf{x}\right)\right\|_2^2 + \lambda P(\mathbf{x}) \tag{9}$$

The ridge penalty is $P(\mathbf{x}) = \left\|\mathbf{L}\mathbf{x}\right\|_2^2$,[4] where $\mathbf{L}$ is a suitable differentiation matrix. For piece-wise linear basis, as in our work, and described in Appendix A, $\mathbf{L}$ can yield up to the first derivative. This penalization term thus minimizes the presence of strong oscillations (ridges) in $\gamma(\tau)$.[5] More generally, by regularizing the least square fitting with the ridge penalty one minimizes both the sum of the regression errors, which describes how well the model fits the data, as well as the sum of the numerical derivatives, which describes how much the regressed data oscillates. Ideally, the ensuing DRT "fits" the data "well" and does not oscillate "too much". The ridge regression is thus used to reduce overfitting in the regression, as the noise is smoothed out by increasing λ. However, this comes at the price of higher bias, since adding more penalty on the derivatives by increasing λ reduces the oscillations of the DRT and concurrently lowers the closeness between the model and the actual data.

The Lasso regression, on the other hand, adds a different penalty, namely, $P(\mathbf{x}) = \|\mathbf{x}\|_1$,[6] given by the sum of the absolute values of the DRT. This penalty results in decreasing the total number of non-zero elements in the DRT [48]. The ensuing regularization thus privileges only a few frequencies of the DRT giving a predominantly discrete time spectrum [44,48]. In the case of the RC circuit, for example, the characteristic timescale response RC will emerge in the DRT.

It is clear that different penalty methods are particularly suited for different applications. For example, a smooth DRT, resulting from distributed timescales, should be analyzed using ridge regression. A discrete DRT, such as the one resulting from an RC circuit or a series of RC circuits should instead be analyzed using Lasso shrinkage. The two can be combined in the same analysis, if no suitable prior for the DRT under study is available, as in the case of this work.

separating the real and imaginary part we obtain the following: $Z_{\text{model}}(f) = R_\infty + \int_{-\infty}^{\infty}\frac{1}{1+(2\pi f)^2e^{2y}}\gamma(y)\mathrm{d}y - i\int_{-\infty}^{\infty}\frac{2\pi fe^{y}}{1+(2\pi f)^2e^{2y}}\gamma(y)\mathrm{d}y$

[2] In the Voigt representation $\phi_n(\ln\tau) = \delta(\tau - \tau_n)$ where τ_n are the collocation points, and $\delta(\tau)$ is the Dirac distribution.

[3] We should note that, as customary in the specialized literature, the $'$ and $''$ symbols indicate the real and imaginary part of the impedance respectively.

[4] $\|\mathbf{x}\|_2 = \sqrt{\sum_{n=1}^{N} x_n^2}$ if $p = 2$, more generally $\|\mathbf{x}\|_p = \sqrt[p]{\sum_{n=1}^{N}|x_n|^p}$ where $p \geq 1$.

[5] Previously, we called the DRT $\gamma(\ln\tau)$ to ease the understanding of the mathematical formulation. From now on, we will adopt the more compact notation $\gamma(\tau)$.

[6] $\|\mathbf{x}\|_1 = \sum_{n=1}^{N}|x_n|$, note that here $p = 1$

2.2. Optimal smoothing for regularized regression

Numerous works in the area of ridge regression have focused on the determination of the best regularization parameter λ. Some of these methods use information regarding the noise. Those include, for example, the unbiased predictive risk estimator [49,50] and Morozov's discrepancy [51]. Other methods do not require such information. Those include generalized cross-validation [52], which minimizes the square of the residual norm divided by the model's number of degrees of freedom, and the L-curve method [53]. The latter method is closely connected to the singular value decomposition of the underlying Fredholm integral operator [54] and it requires the identification of the turning point of the L-curve[7]. Other methods extract the information contained in the residual vector using the Fourier transform, subsequently plotting the residual and its cumulant versus frequency in order to check its statistical properties [55,56].

In spite of the abundance of methods, they have shortcomings when applied to EIS data. For example, the noise level is hardly ever known a priori, convergence may not be guaranteed [57], many local minima may emerge [58,59], or the error structure may violate the normality hypothesis [56].

Similarly, parameter selection algorithms are also possible for the Lasso for example via n-fold cross-validation [44,60]. By using this method the Lasso solution is computed from several subsets of the data, the so-called training sets, and the obtained value is tested against other data subsets, the so-called test sets [61]. The implementation of this test may present some challenges in the electrochemical context due to the small data set's size available in EIS. In fact, the identification of a training set and a validation set within the EIS spectrum would be required.

In this work we develop two alternative methods: a real and imaginary discrepancy test and a real and imaginary cross-validation test. The former evaluates whether the results obtained by the real and imaginary part of the data match. The latter addresses whether the DRT obtained using only the imaginary/real part of the data can match the real/imaginary part of the impedance data. The underlying idea of the latter criterion is similar to the Kramers-Kronig transform method [62,63], which measures the consistency between the real and imaginary part of the spectrum. We propose to jointly use both test functions as shown in the scheme of Fig. 3. As illustrated in the upper part of the scheme, the DRT is determined by separately considering the real and the imaginary part of the EIS measurement. Afterwards, as shown in the lower part of the scheme, the two DRT independently obtained are compared through the minimization of test functions mentioned above. Each minimization returns an optimal value of the regularization parameter λ.

2.2.1. Re-Im discrepancy test function

The idea behind the real and imaginary discrepancy test function, simply referred to as "Re-Im discrepancy", is to assess the discrepancy between the DRT computed using independently the real, and the imaginary parts of the data. We define the Re-Im discrepancy as the distance between the real and imaginary part of the deconvolved DRT as

$$\text{discrepancy}(\lambda) = \left\|\mathbf{x}'' - \mathbf{x}'\right\|_2^2 \tag{10}$$

where $\mathbf{x}'$ and $\mathbf{x}''$ are the DRT vectors computed by minimizing (9) respectively with $\boldsymbol{\Omega}'' = 0$ and $\boldsymbol{\Omega}' = 0$. The smaller is the discrepancy function, the closer the two computed DRT are. This ensures the consistency between the DRT obtained using the real part of the data against the one acquired from the imaginary part.

2.2.2. Re-Im cross-validation test functions

We define a real and imaginary cross-validation test, simply referred to as "Re-Im cross-validation", which accesses the distance between the real/imaginary part of the experimental impedance and the impedance computed using the DRT of the imaginary/real part of the measured impedance. Physically, this corresponds to testing how well the approximate $\gamma(\tau)$ obtained using imaginary/real data matches the real/imaginary data. Thus, we define three validation functions. The first is

$$\text{Re-}Im \quad cross\text{-}validation'(\lambda) = \left\|\mathbf{Z}'_{\text{exp}} - \mathbf{A}'\mathbf{x}''\right\|_2^2 \tag{11}$$

where $\left(\mathbf{Z}'\right)_j = Z'(f_j)$ and $\mathbf{x}''$ is the DRT computed by minimizing (9) with $\boldsymbol{\Omega}' = 0$, and

$$\text{Re-}Im \quad cross\text{-}validation''(\lambda) = \left\|\mathbf{Z}''_{\text{exp}} - \mathbf{A}''\mathbf{x}'\right\|_2^2 \tag{12}$$

where $\left(\mathbf{Z}''\right)_j = Z''(f_j)$ and $\mathbf{x}'$ is the DRT computed by minimizing (9) with $\boldsymbol{\Omega}'' = 0$. We also define the Re-Im cross-validation sum as

$$\text{Re-}Im \quad cross\text{-}validation(\lambda) = \text{Re-}Im cross\text{-}validation'(\lambda) + \text{Re-}Im \quad cross\text{-}validation''(\lambda) \tag{13}$$

The lower is the validation error, the better the real/imaginary DRT will predict the imaginary/real part of the impedance spectrum. Also, this is a physically plausible measure of the quality of the DRT fit.

3. Results

Here, we discuss three synthetic experiments and three real experiments. We study the synthetic experiments to test our approach against situations where the analytical DRTs are available. This allows us to compute the exact regularization error and to rank the criteria that can be used to obtain the "best" λ. Next, we study three experimentally relevant cases, which allow us to link the computational/theoretical results to the electrochemical practice.

3.1. Synthetic experiments

First, we perform synthetic experiments by employing an analytical impedance $Z(f)$ with known DRT response and we corrupt it using randomly generated noise as follows [64–67]

$$Z_{\text{exp}}(f) = Z(f) + \varepsilon|Z(f)|(\eta' + i\eta'') \tag{14}$$

where $\varepsilon = 0.5\%$, and η' and η'' are two independent identically distributed Gaussian process with mean 0 and standard deviation 1, i.e., $\eta' \sim \mathcal{N}(0, 1)$ and $\eta'' \sim \mathcal{N}(0, 1)$.

Our qualitative analysis uses three different circuits with known DRT: an RC circuit, a ZARC element, and a fractal element. To bridge between synthetic and real experiments, we also tested a symmetric cell, whose impedance response can be modeled as a series of ZARC elements [70], see Sec. 3.2.1, as well as a collection of RC circuits, which was provided by the manufacturer along with our potentiostat system, see Sec. 3.2.2.

3.1.1. RC circuit

The impedance response of the RC circuit is given by

$$Z(f) = R_\infty + \frac{R}{1 + i2\pi fRC} \tag{15}$$

[7] The L-curve plots in log-log scale the residual norm against the norm of the actual solution.

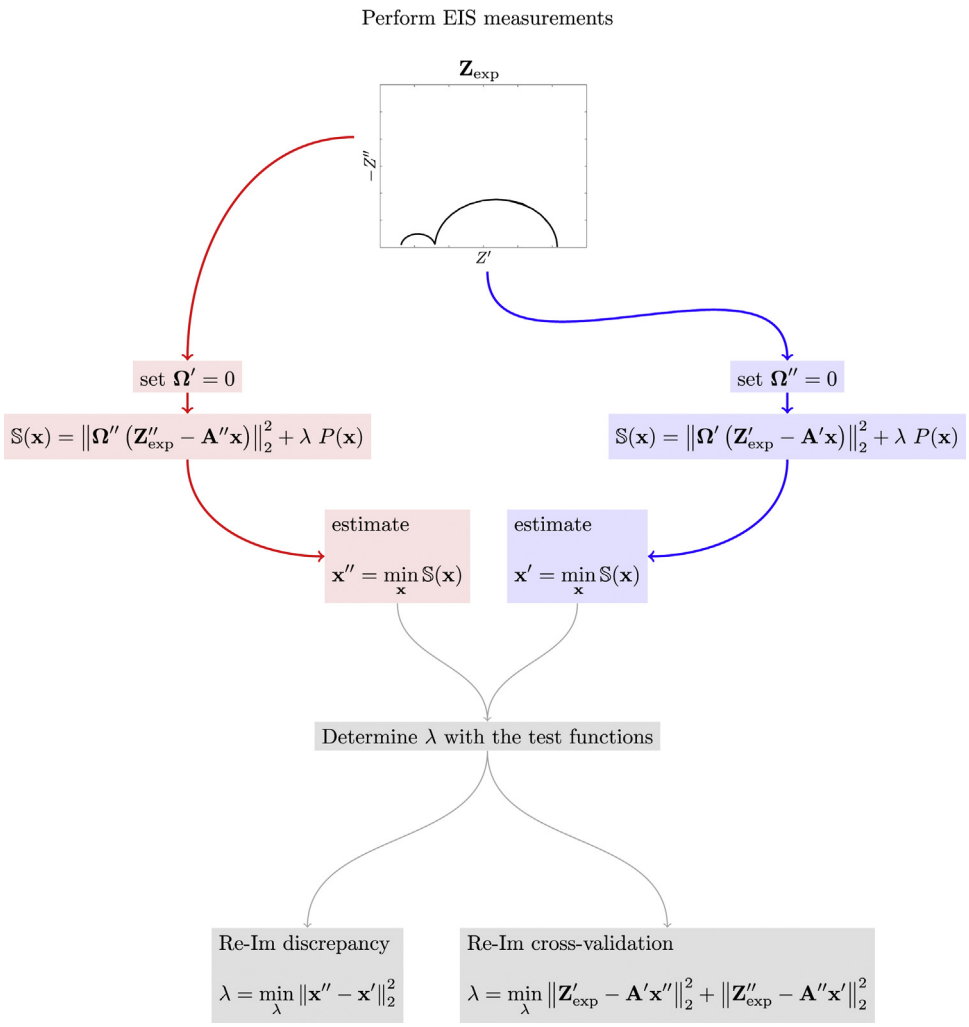

Fig. 3. Flow diagram for the sequential algorithm used to determine the optimal regularization parameter λ. Examples of the Re-Im discrepancy and Re-Im cross-validation plotted as function of λ as shown in Fig. 8.

where we take $R_\infty = 1\ \Omega$, $R = 1\ \Omega$ and $C = 1$ F. We compare the reconstructed DRT obtained using (5) and (9) against the exact DRT, which for (15) corresponds to $\gamma(\tau) = R\delta(\ln \tau)$, i.e., a Dirac distribution (multiplied by R) centered at $\tau = 1$ s. Fig. 4 shows the results of the regularized inversion using ridge regression, panel (a), and Lasso regression, (b). The ridge regression smooths out the computed DRT by decreasing the norm of the first derivative with increasing λ. Hence, as shown in Fig. 4a, a large λ flattens out the

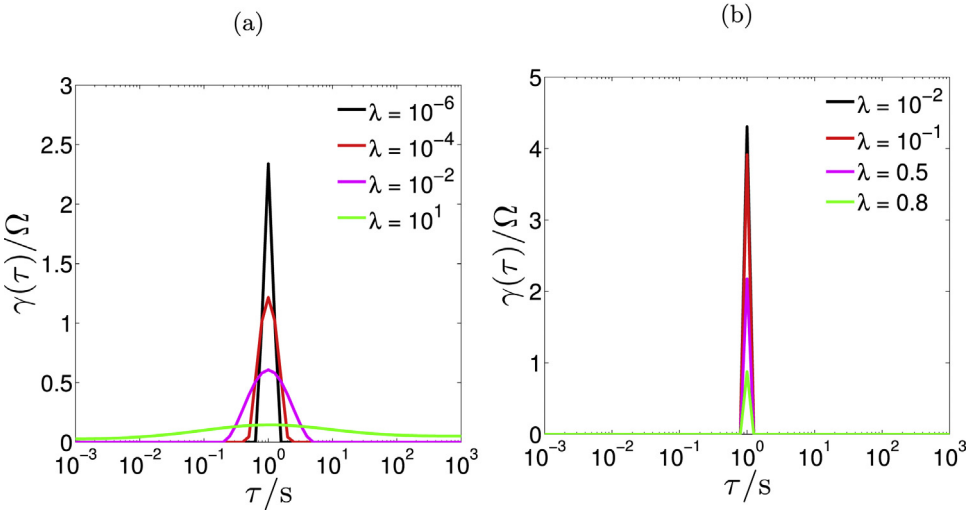

Fig. 4. DRT of the RC circuit using the ridge regression, (a), and the Lasso regression, (b).

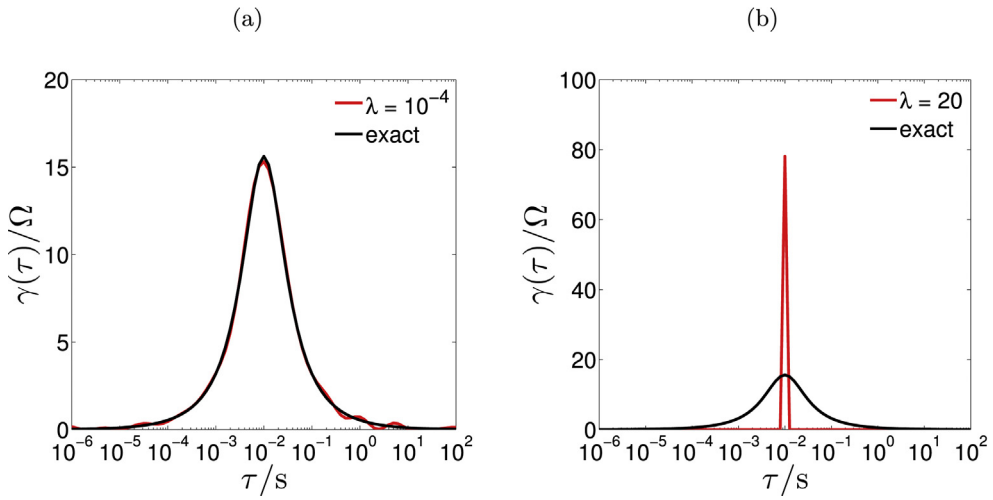

Fig. 5. DRT of the ZARC circuit using the ridge regression, (a), and the Lasso regression, (b).

DRT, thereby reducing the DRT sensitivity to measurement errors; while a smaller λ concentrates the impedance to a sharp peak. The Lasso regression, on the other hand, penalizes the $\sum_{n=1}^{N}|x_n|$ thereby decreasing the overall sum of non-zero terms and emphasizing over a minimal set of relevant frequencies. This is also the case here, see Fig. 4b, where, by increasing λ, the total number of nonzero elements decreases and the maximum value of the DRT response decreases. If the λ is too small, then less regularization is given and more peaks can be found as a result of the noise in the data.

3.1.2. ZARC element

We further extend this qualitative analysis to the ZARC circuit, which comprises a resistance in series with the parallel connection of a resistor and a constant phase element (CPE). The ZARC element is characterized by the impedance response

$$Z(f) = R_\infty + \frac{R_{ct}}{1 + (i2\pi f\tau_0)^\phi} \tag{16}$$

where we take $R_\infty = 10\,\Omega$, $R_{ct} = 50\,\Omega$, $\tau_0 = 0.01$ s, and $\phi = 0.7$. The DRT corresponding to the Z_{ZARC} above is given by [23]

$$\gamma(\tau) = \frac{R_{ct}}{2\pi}\frac{\sin((1-\phi)\pi)}{\cosh\left(\phi\ln\left(\frac{\tau}{\tau_0}\right)\right) - \cos((1-\phi)\pi)} \tag{17}$$

We can compare the exact DRT with the value of the reconstructed DRT. The latter was obtained by fitting the impedance data using ridge and Lasso regression as shown in Fig. 5a and Fig. 5b respectively. By carefully selecting the regularization value λ, the ridge regression closely matches the exact impedance. Differently, the Lasso regression does not match the exact impedance, but it correctly localizes the peak of $\gamma(\tau)$.

3.1.3. Fractal element

We also study the fractal element, a somewhat pathological circuit characterized by a discontinuous DRT. Its impedance response is given by

$$Z(f) = R_\infty + \frac{R_{ct}}{(1 + i2\pi f\tau_0)^\phi} \tag{18}$$

where $R_\infty = 10\,\Omega$, $R_{ct} = 10\,\Omega$, $\phi = 0.6$ and $\tau_0 = 0.1$ s. The DRT has an analytical expression of the following form

$$\gamma(\tau) = \begin{cases} R_{ct}\dfrac{\sin(\phi\pi)}{\pi}\left(\dfrac{\tau}{\tau_0 - \tau}\right)^\phi & \text{if} \quad \tau < \tau_0 \\ 0 & \text{if} \quad \tau > \tau_0 \end{cases} \tag{19}$$

where τ_0 is the location of the discontinuity of $\gamma(\tau)$. Similarly to what was done in the previous two cases, we can compare the exact DRT for the fractal element with the value obtained for the reconstructed DRT by fitting the impedance using ridge regression as shown in Fig. 6a. The ridge regression may not be able to closely

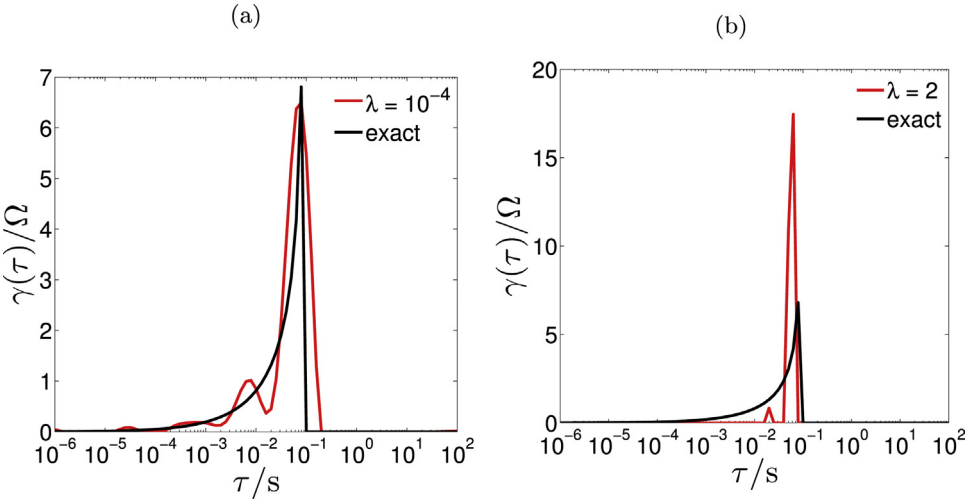

Fig. 6. DRT of the fractal circuit using the ridge regression, (a), and the Lasso regression, (b).

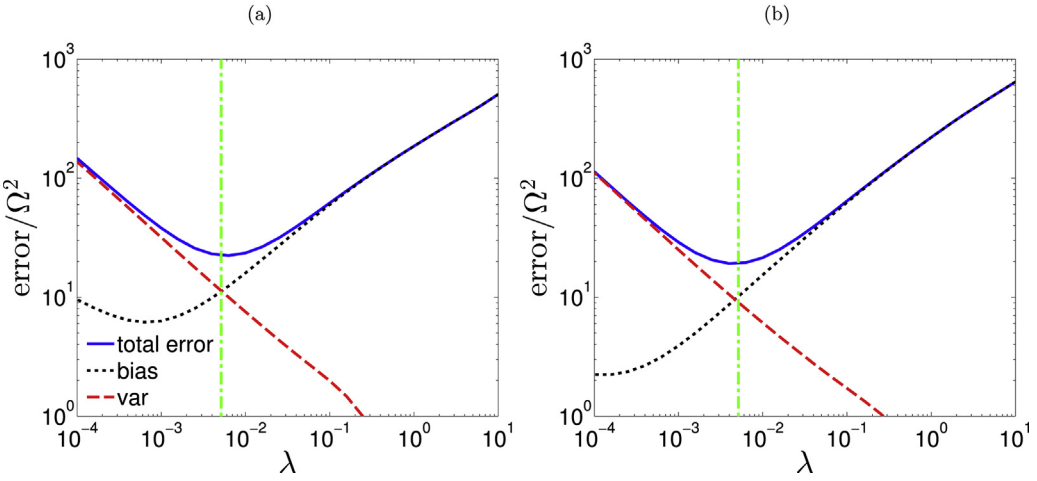

Fig. 7. The bias-variance trade-off for the regularized **x** computed using the real part, (a), and imaginary part, (b), of the data. The vertical dashed line is placed at the minimum of the sum of the real and imaginary data total error. The relevant quantities are computed using 1000 Monte Carlo samples.

capture the non-continuity of the exact DRT due to the enforcement of the regularity condition. The reconstructed DRT for $\lambda = 10^{-4}$ highlights this issue. In a similar manner, the Lasso regression shown in Fig. 6b only captures one of the DRT's features, focusing the regressed $\gamma(\tau)$ at the discontinuity of the exact DRT.

3.1.4. Bias-variance trade-off

We perform a set of $M = 1000$ synthetic experiments using the noise-corrupted virtual measurement given by (14) with model (16). We then compute the DRT for all simulated experiments for a given range of regularization parameters λ by (9) and we compare the computed DRT with its exact counterpart as a function of λ itself. In that context we plot three relevant quantities which are functions of the exact DRT $\mathbf{x}_{\text{exact}}$ taken at the frequencies $f_1, f_2, \ldots, f_M$ as well as of the $\mathbf{x}_m(\lambda)$, that is the result of the ridge regression with smoothing parameter λ obtained using the m^{th} (out of M) synthetic experiment. The first relevant quantity is the total error defined as the expected distance between the exact DRT and the calculated DRT:

$$E_{\text{tot}}(\lambda) \approx \frac{1}{M}\sum_{m=1}^{M}\left\|\mathbf{x}_{\text{exact}} - \mathbf{x}_m(\lambda)\right\|_2^2 \tag{20}$$

The second quantity is the average bias defined as the distance between the exact DRT and the average regressed, or expected, DRT, that is

$$E_{\text{bias}}(\lambda) \approx \left\|\mathbf{x}_{\text{exact}} - \frac{1}{M}\sum_{m=1}^{M}\mathbf{x}_m(\lambda)\right\|_2^2 \tag{21}$$

We can also define a third quantity as the variance of the DRT, defined as

$$E_{\text{var}}(\lambda) \approx \frac{1}{M}\sum_{m=1}^{M}\left\|\mathbf{x}_m(\lambda) - \frac{1}{M}\sum_{m=1}^{M}\mathbf{x}_m(\lambda)\right\|_2^2 \tag{22}$$

The $E_{\text{tot}}(\lambda)$ is the sum of the bias of our average DRT and the variance of the DRT:

$$E_{\text{tot}}(\lambda) = E_{\text{bias}}(\lambda) + E_{\text{var}}(\lambda) \tag{23}$$

The $E_{\text{tot}}(\lambda)$ has a minimum corresponding to an optimal trade-off between bias and variance at a given λ. The $E_{\text{bias}}(\lambda)$ is an increasing function of λ, while the variance is monotonically decreasing. This is easily reconciled with intuition since the greater is λ, the greater the smoothing is, and the flatter the reconstructed $\gamma(\tau)$ will be. While this decreases the effects of oscillations due to the noise in the system hereby decreasing the $E_{\text{var}}(\lambda)$, it increases the bias, since the exact and the average reconstructed $\gamma(\tau)$ will depart more significantly at greatest λ. These two competing effects lead to a minimum in total error. This intuitive trade-off concept is shown for the case of the ZARC using the real and imaginary portion of the impedance, see Fig. 7a and 7b respectively. The minimum of the sum of the real and imaginary errors, which is indicated by the dashed vertical line, is located at $\lambda \approx 0.05$.

We then compare the total error behavior with the Re-Im discrepancy and Re-Im cross-validation as a function of λ. This allows us to see which test functions better serves its purpose. The Re-Im discrepancy, which measures how far the $\gamma(\tau)$'s computed separately using the real and imaginary part of the data, ensure maximal consistency between the results. It can be seen in Fig. 8a that when averaged over $M = 1000$ synthetic experiments, the maximal consistency or minimal Re-Im discrepancy is found for $\lambda \approx 0.25$ corresponding to a condition where the bias is the main contributor to the total error. The Re-Im cross-validation, which checks instead whether the $\gamma(\tau)$ computed using the real/imaginary data is able to fit the imaginary/real part of the impedance, shows in Fig. 8b a shallow minimum at $\lambda \approx 0.025$ and $\lambda \approx 0.063$ for the real and imaginary part respectively. It is clear that this second value is much closer to the regression parameter value minimizing the $E_{\text{tot}}(\lambda)$.

3.2. Experimental results

We studied the DRT of three electrochemical experiments. The first system is a symmetric cell composed of ceramics used in solid oxide fuel cells (SOFC), the second system is a collection of RC circuits, and the last system is an off-the-shelf Li-ion battery. These are reported in Fig. 9a, Fig. 9b and Fig. 9c, respectively. The RC circuit and the battery were studied at room temperature, while the symmetric cell was tested at 700 °C. The electrochemical impedance spectroscopy data were obtained using a VSP test station (Bio-Logic Science Instruments SAS, France).

3.2.1. Symmetric fuel cell

The symmetric cell consists of a 15% Samarium-doped Ceria (SDC) electrolyte, coated with a symmetrical layer of $SrNb_{0.1}Co_{0.9}O_{3-\delta}$ (SNC) through pulsed laser deposition (PLD). The SDC powder was obtained using the process presented in [68]. The SNC powder was synthesized using the same procedure described elsewhere [69], while the deposition details are identical to those

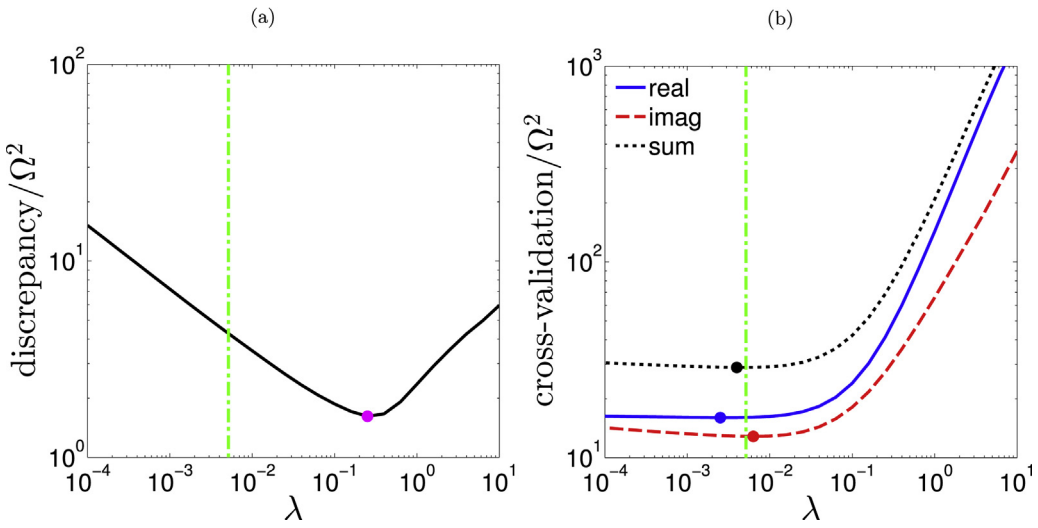

Fig. 8. The Re-Im discrepancy function, (a), and Re-Im cross-validation functions, (b), plotted against the regularization parameter λ. The total error minimum dash-dot line is shown for reference. The minimum of the Re-Im discrepancy function is shown as a dot in (a). The minimum of the real, imaginary and total Re-Im cross-validation functions are also shown in (b).

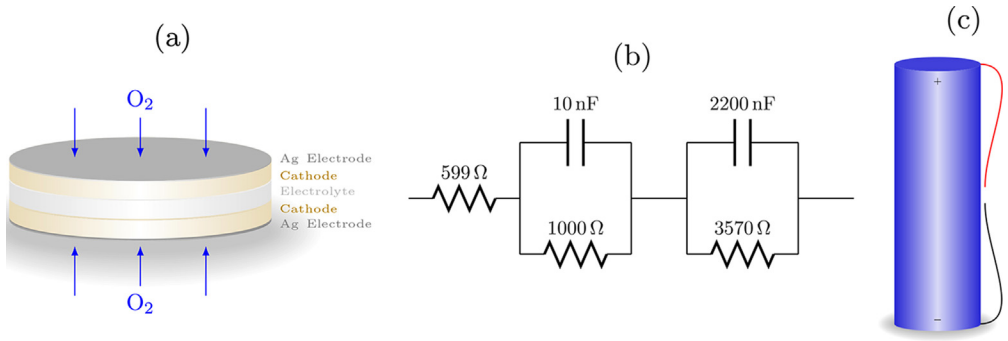

Fig. 9. Illustrations of the systems being tested. Illustration of the symmetric cell, (a), schematic representation of the RC circuits, (b), and image of the commercial Li-ion battery, (c).

outlined in an earlier publication [70]. The silver leads were symmetrically painted on SNC and the experiment was conducted in a fuel cell test station at 700 °C in a 21%-79% mixture of O_2 and N_2. A total of 100 EIS spectra were recorded with 5 points per decade logarithmic spacing for f from 40 kHz to 0.5 Hz. In order to summarize this large set of data, the average EIS is shown as a solid red line (the relevant frequencies are marked as black dots) in Nyquist form in Fig. 10, and the 3σ confidence bands are highlighted in grey, indicating that the real data is noisy. In the present work we omit the equivalent circuit fitting for the symmetric cell. However, an approach based on complex nonlinear least square fitting based on similar data was presented in a previous work [70].

In Fig. 11a, we show the results of the Re-Im discrepancy and Re-Im cross-validation as functions of λ for all experimental data. The average values of these two functions are presented in conjunction with their 3σ bands. It can be seen that the variability of the Re-Im cross-validation is reduced in comparison to the Re-Im discrepancy. The average minimum Re-Im discrepancy is found at $\lambda \approx 0.22$, while the average minimum Re-Im cross-validation function is obtained at $\lambda \approx 0.056$. This yields a distribution of the minima $p(\log_{10}\lambda)$[8] as

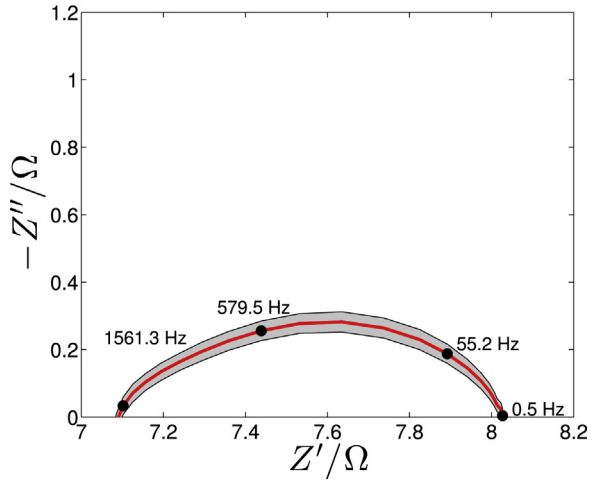

Fig. 10. Experimental impedance data of the symmetric cell composed of ceramics used in SOFC. The average EIS is shown with a solid red line along with the experimental 3σ confidence band in the shaded grey region.

reported in Fig. 11b, which are again centered at the values reported above.

The corresponding DRT obtained through ridge regression are reported in Fig. 12a and Fig. 12b, which were obtained by

[8] Technically this is the empirical probability density function of the minima of the Re-Im discrepancy and the Re-Im cross-validation with respect to $\log_{10}\lambda$.

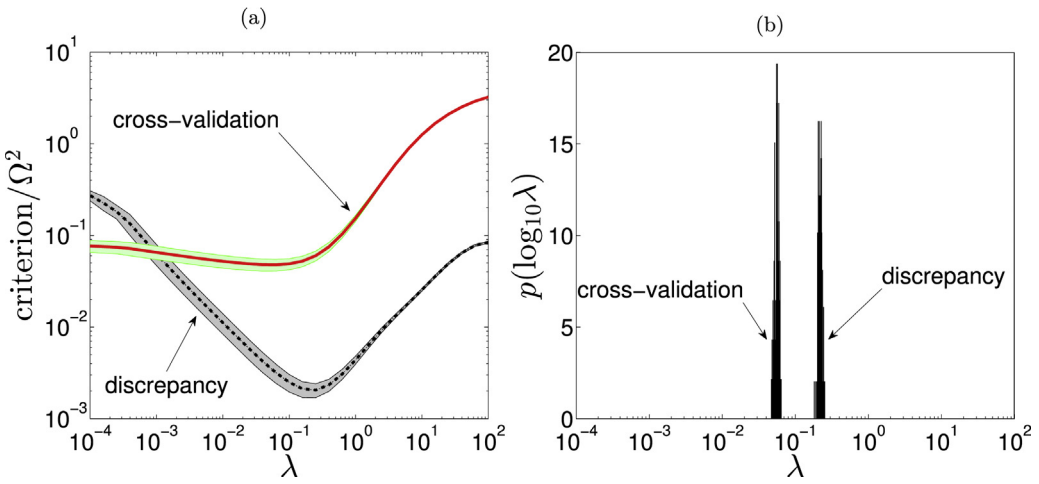

Fig. 11. Re-Im discrepancy and Re-Im cross-validation functions computed for the symmetric cell, (a). The empirical probability density function of the minimum of the Re-Im discrepancy and Re-Im cross-validation function, (b).

minimizing the Re-Im discrepancy and the Re-Im cross-validation respectively. We should note that the average DRT is shown along with its 3σ band. Simple visual inspection suggests that the resulting DRT convolves two processes. The results of the average Lasso regression with $\lambda = 0.4$ is presented in Fig. 12c as a red line along with its 3σ bands. The result confirms the presence of two distinct characteristic times.

3.2.2. Collection of RC circuits

A collection of RC circuits was tested and its schematic representation is presented in Fig. 9b. The actual timescales of the system (RC) are $\tau = 7.85 \cdot 10^{-3}$ s and $\tau = 1 \cdot 10^{-5}$ s. The experimental data corresponding to 100 EIS spectra are plotted in the Nyquist plot in Fig. 13. The data were obtained through EIS scans for f from 200 kHz to 0.1 Hz with 10 points per decade. The average

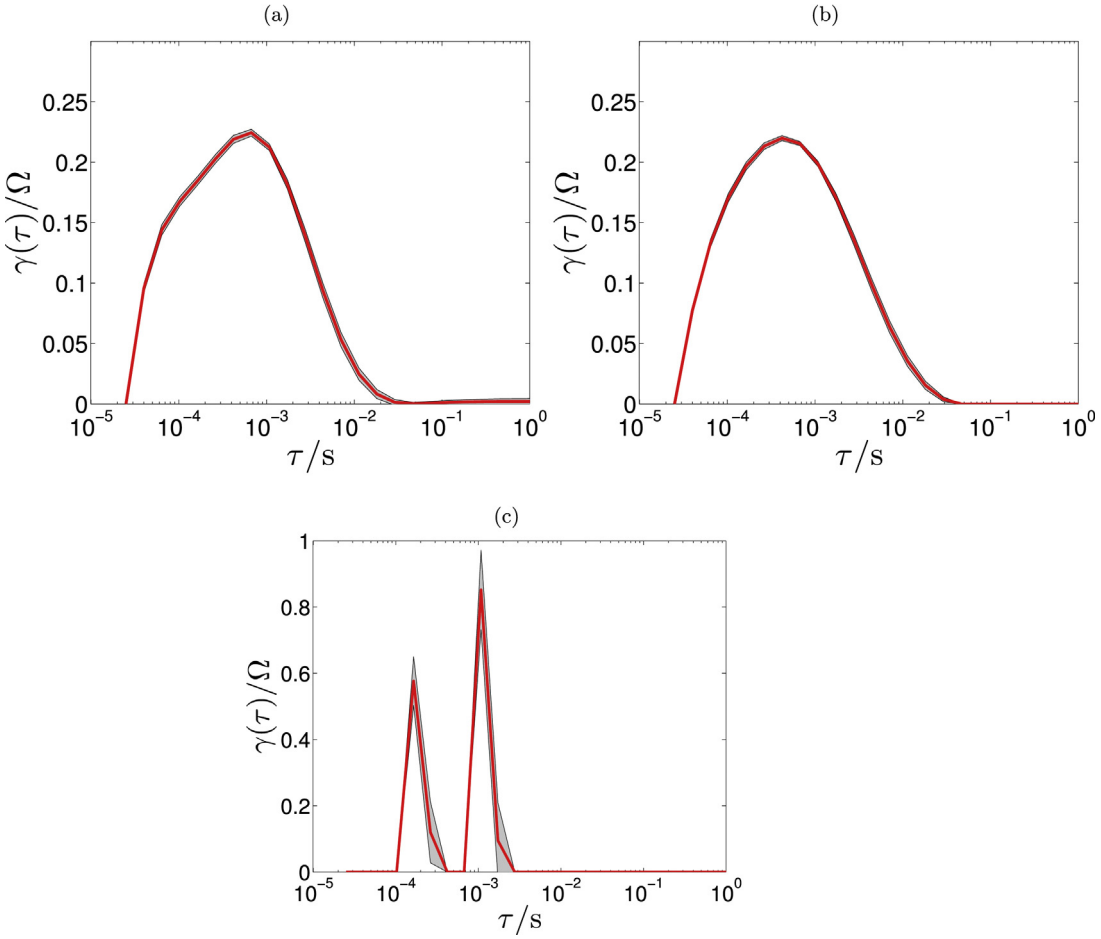

Fig. 12. DRT results of the ridge minimizing the Re-Im discrepancy function, (a), and the Re-Im cross-validation function, (b). The result applying Lasso regression is shown in (c). The DRT is computed from the imaginary part of the impedance data of the symmetric cell. The average DRTs are shown with a solid red line along with the 3σ confidence band represented by the shaded grey region.

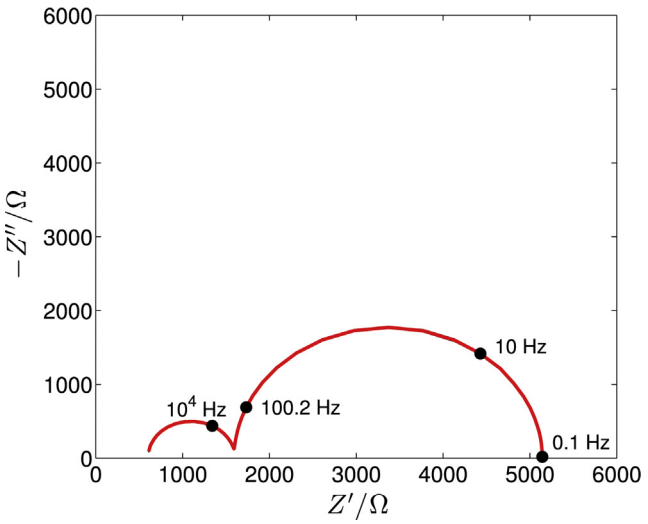

Fig. 13. Experimental impedance data of the RC circuit. The average EIS is shown with a solid red line in combination with the experimental 3σ confidence band represented by the shaded grey region.

EIS is shown with a solid red line and the 3σ confidence band is highlighted in grey, indicating that the real data is highly reproducible.

The corresponding average DRT obtained through ridge regression is reported in Fig. 14 along with its 3σ band. The ridge regression is shown at $\lambda \approx 8.15 \cdot 10^{-9}$, a value minimizing the Re-Im cross-validation function, in panel (a), as well as $\lambda \approx 0.091$, minimizing the Re-Im discrepancy, panel (b). In both cases, the resulting DRT correctly identifies the range of the relevant processes. While the Re-Im cross-validation results in a DRT highlighting only one narrow frequency set, the Re-Im discrepancy case spreads the DRT to a broader set of frequencies as in the case of the ZARC element of subsec. 3.1.2. These results can be complemented by the Lasso regression ($\lambda = 0.1$), shown in panel (c), which capture again the discrete nature of the experimental system suggesting that in this case the minimization of the Re-Im discrepancy is a more suitable criterion.

3.2.3. Li-ion battery

Lastly, we studied the EIS response of a commercial Li-ion cell ($LiCoO_2$–Ansmann 18650) with a nominal capacity of 2250 mAh. To the best of our knowledge only few applications of DRT to Li-ion batteries exist in the literature [37,71], despite the need

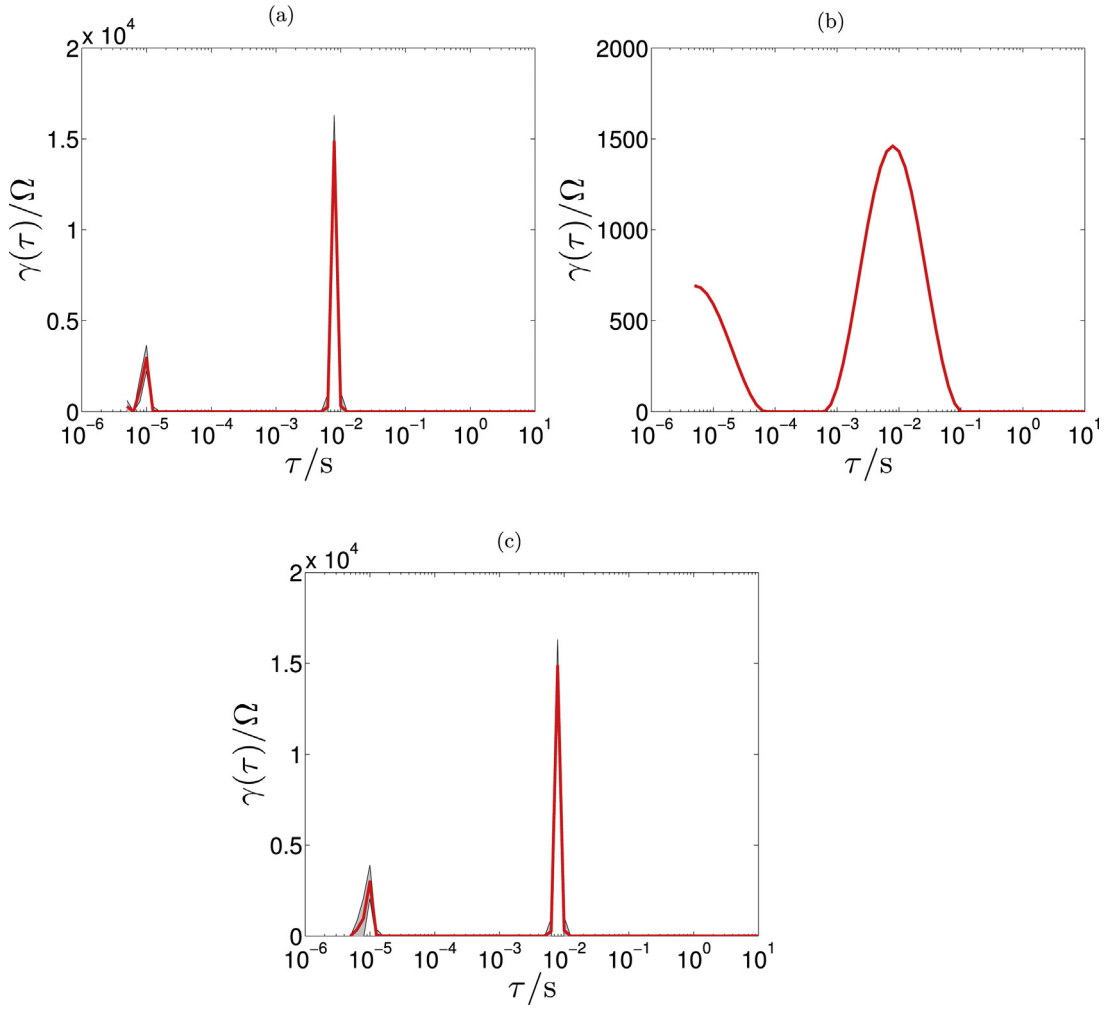

Fig. 14. DRT results computed with the imaginary part of the experimental data of the RC circuit using ridge regression at minimum Re-Im cross-validation ($\lambda \approx 8.15 \cdot 10^{-9}$), (a), at minimum Re-Im discrepancy ($\lambda \approx 0.091$), (b), and Lasso regression($\lambda = 0.1$), (c). The average DRTs are shown with a solid red line along with the 3σ confidence band represented by the shaded grey region.

for non-destructive electrochemical characterization methods for these devices. We tested the battery at a State of Charge (SOC) of 25%. The data corresponding to the EIS spectra are plotted in banded Nyquist form in Fig. 15. The data were acquired for f between 600 Hz and 50 mHz with 10 points per decade. Due to the long testing time, only 12 EIS spectra were recorded.

The corresponding DRT obtained through ridge and Lasso regression under optimal conditions are reported in Fig. 16. The ridge regression was performed at the value of λ, which minimizes the Re-Im cross-validation function ($\lambda \approx 6.02 \cdot 10^{-5}$), panel (a), and the Re-Im discrepancy function ($\lambda \approx 9.1$), panel (b). In the first case, the resulting DRT identifies four different processes. The latter case, on other hand, identifies only three processes and presents a higher degree of smoothing. The results of the Lasso regression are also displayed, panel (c); this was performed using a value of $\lambda = 5 \cdot 10^{-4}$. The Lasso highlights the presence of several peaks which are roughly centered at the same location of peaks obtained via the ridge regression. In the Lasso results, a stronger oscillation of the solution in terms of its average value as well as of the 3σ bounds is also present. This behavior is due to the complex nature of the Li-ion battery electrochemistry. Overall, the results suggest that the minimization of the Re-Im discrepancy function is a suitable criterion and the Lasso regression should be used in conjunction with the ridge regression in order to mark the relevant timescales and their peaks during the analysis.

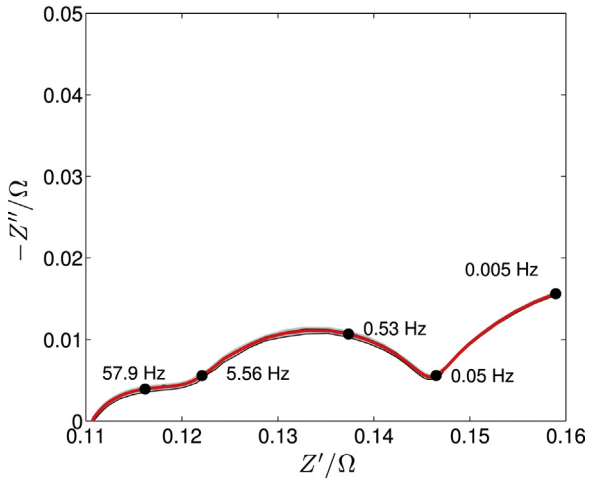

Fig. 15. Experimental impedance data of a Li-ion battery. The average EIS is shown with a solid red line in conjunction with the experimental 3σ confidence band represented by the shaded grey region.

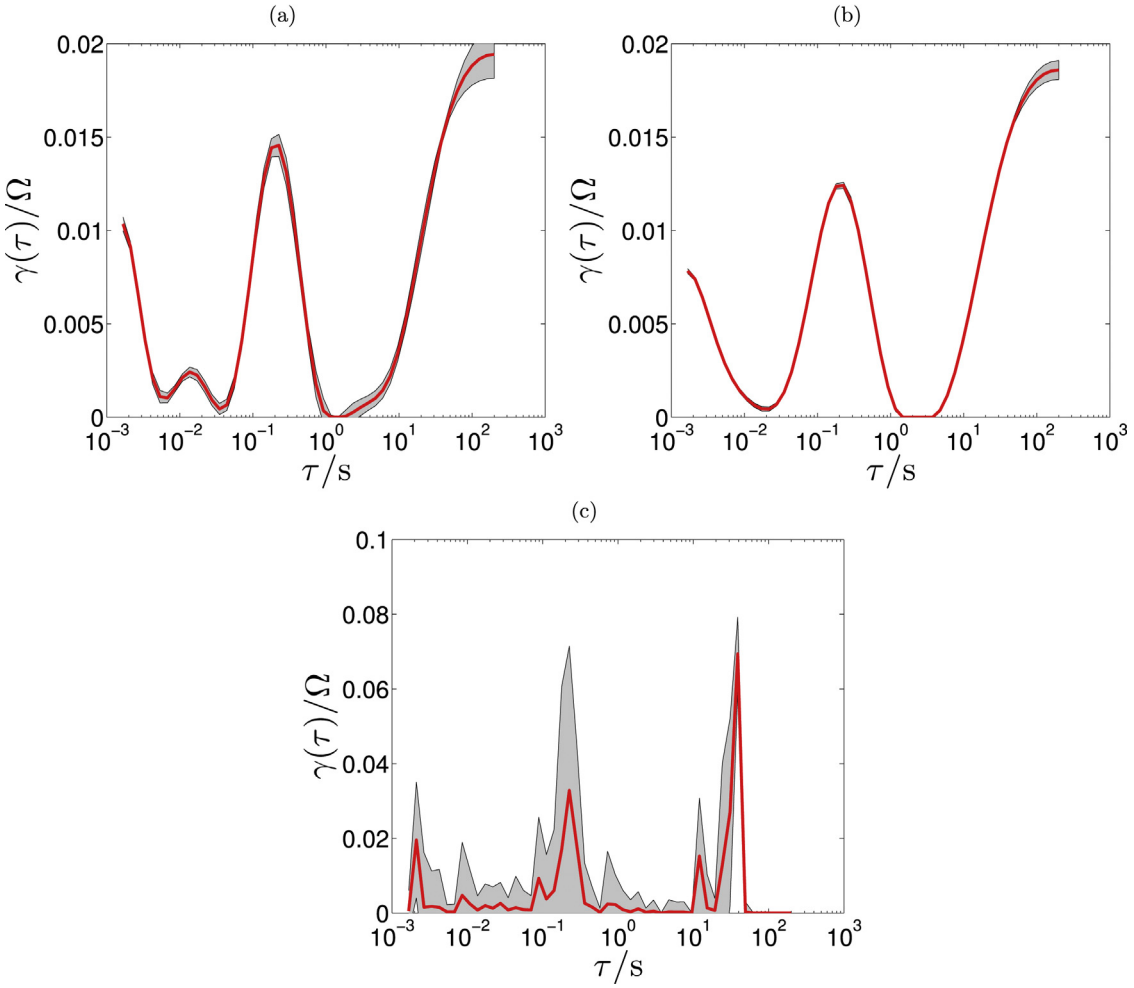

Fig. 16. DRT results computed with the imaginary part of the experimental data of the Li-ion battery using ridge regression at Re-Im minimum cross-validation function ($\lambda \approx 6.02 \cdot 10^{-5}$), (a), at minimum Re-Im discrepancy function ($\lambda \approx 9.1$), (b), and Lasso regression ($\lambda = 5 \cdot 10^{-4}$), (c). The average DRTs are shown with a solid red line along with the 3σ confidence band represented by the shaded grey region.

4. Conclusions

This work discusses the application of regularized DRT to EIS data to obtain the relevant timescales when studying an electrochemical system. In particular, we introduced two new test functions for the identification of the optimal regularization parameter λ in the case of ridge regression and we benchmarked our results using the Lasso regression.

Via the use of synthetic and real experiments, we evaluated the performance of the proposed Re-Im discrepancy and the Re-Im cross-validation tests in presence of known exact DRT functions and in real electrochemical applications. According to the results, the minimization of the Re-Im cross-validation functions is good criteria for finding the optimal degree of regularization. It appears, however, that both Re-Im discrepancy and the Re-Im cross-validation should be utilized and the resulting DRTs should be critically compared. Particularly, the Lasso regression should be used in conjunction with the ridge regression in order to mark the relevant peaks, or timescales, in the analysis. In this regard, the simultaneous use of both ridge and Lasso regularization should be investigated in the future. One possible approach is called elastic net, which applies a linear combination of ridge and Lasso regularization, i.e., $\alpha\|\mathbf{x}\|_1 + (1-\alpha)\left\|\mathbf{L}\mathbf{x}\right\|_2^2$.

While this work focused primarily on ridge/Lasso regression applied to DRT, we would like to conclude by commenting that many open questions regarding DRT deconvolution still need to addressed. In particular, speed and accuracy benchmarks for the various methods, including ridge/lasso regression, Fourier filtering, Monte Carlo, maximum entropy, and genetic programming, may be beneficial. Such benchmarks should be the object of future work.

Acknowledgments

The authors gratefully acknowledge HKUST for providing start-up funds, and the Research Grants Council of Hong Kong for support through the projects DAG12EG06, and ECS 639713. M.S. acknowledges the support of the Hong Kong PhD Fellowship Scheme.

Appendix A. Numerical Formulation

In this article we solve

$$\mathbb{S}(\mathbf{x}) = \sum_{n=1}^{N}\left[\frac{1}{w_n'}\left(Z'_{\exp}(f_n) - \left(\mathbf{A}'\mathbf{x}\right)_n - R_\infty\right)^2 + \frac{1}{w_n''}\left(Z''_{\exp}(f_n) - \left(\mathbf{A}''\mathbf{x}\right)_n\right)^2\right] + \lambda P(\mathbf{x}) \tag{A.1}$$

where $P(\mathbf{x}) = \left\|\mathbf{L}\mathbf{x}\right\|_2^2 = \sum_{n=1}^{N-1}((\mathbf{L}\mathbf{x})_n)^2$ or $P(\mathbf{x}) = \|\mathbf{x}\|_1 = \sum_{n=1}^{N}|x_n|$ with the constraint that $x_n \geq 0$. Also note that we order the frequencies such that $f_1 \geq f_2 \geq \ldots \geq f_N$, in order to give $\tau_1 \leq \tau_2 \leq \ldots \leq \tau_N$. It should noted that the matrix $\mathbf{L}$ is defined as a $(N-1)\times N$ first derivative differentiation matrix

$$\mathbf{L} = \begin{bmatrix} -\frac{1}{\Delta_1} & \frac{1}{\Delta_1} & & 0 \\ & \ddots & \ddots & \\ 0 & & -\frac{1}{\Delta_{N-1}} & \frac{1}{\Delta_{N-1}} \end{bmatrix} \tag{A.2}$$

where $\Delta_n = \ln\frac{\tau_{n+1}}{\tau_n} = \ln\frac{f_n}{f_{n+1}} \geq 0$. Thus, $(\mathbf{L}\mathbf{x})_n$ approximates the first derivative of the function $\gamma(\ln\tau)$ with respect to $\ln\tau$ at $\tau_n = \frac{1}{f_n}$. Incidentally, it should be noted that one can only define a first order derivative when a piecewise linear basis is used.

Furthermore, the matrix $\mathbf{A}$ approximates the two integrals on the right hand side of (6), namely,

$$\left(\mathbf{A}'\right)_{n,m} \approx \int_{-\infty}^{\infty}\frac{1}{1+(2\pi f_n\tau)^2}\phi_m(\ln\tau)\ \mathrm{d}\ln\tau \tag{A.3a}$$

$$\left(\mathbf{A}''\right)_{n,m} \approx -\int_{-\infty}^{\infty}\frac{2\pi f_n\tau}{1+(2\pi f_n\tau)^2}\phi_m(\ln\tau)\ \mathrm{d}\ln\tau \tag{A.3b}$$

If a piecewise finite element basis is chosen, then one may approximate the matrices $\mathbf{A}'$ and $\mathbf{A}''$ as follows:

$$\left(\mathbf{A}'\right)_{n,m} = \begin{cases} \frac{1}{2}\frac{1}{1+(2\pi f_n\tau_m)^2}\ln\frac{\tau_{m+1}}{\tau_m} & \text{if} \quad m=1 \\ \frac{1}{2}\frac{1}{1+(2\pi f_n\tau_m)^2}\ln\frac{\tau_m}{\tau_{m-1}} & \text{if} \quad m=N \\ \frac{1}{2}\frac{1}{1+(2\pi f_n\tau_m)^2}\ln\frac{\tau_{m+1}}{\tau_{m-1}} & \text{otherwise} \end{cases} \tag{A.4}$$

$$\left(\mathbf{A}''\right)_{n,m} = \begin{cases} -\frac{1}{2}\frac{2\pi f_n\tau_m}{1+(2\pi f_n\tau_m)^2}\ln\frac{\tau_{m+1}}{\tau_m} & \text{if} \quad m=1 \\ -\frac{1}{2}\frac{2\pi f_n\tau_m}{1+(2\pi f_n\tau_m)^2}\ln\frac{\tau_m}{\tau_{m-1}} & \text{if} \quad m=N \\ -\frac{1}{2}\frac{2\pi f_n\tau_m}{1+(2\pi f_n\tau_m)^2}\ln\frac{\tau_{m+1}}{\tau_{m-1}} & \text{otherwise} \end{cases} \tag{A.5}$$

Lastly, we obtain (9) by defining the following two matrices

$$\left(\boldsymbol{\Omega}'\right)_{n,m} = \frac{1}{\sqrt{w'_{n,m}}}\delta_{n,m} \quad \text{where} \quad n=1,\ldots,N \quad \text{and} \quad m=1,\ldots,M \tag{A.6a}$$

$$\left(\boldsymbol{\Omega}''\right)_{n,m} = \frac{1}{\sqrt{w''_{n,m}}}\delta_{n,m} \quad \text{where} \quad n=1,\ldots,N \quad \text{and} \quad m=1,\ldots,M \tag{A.6b}$$

Lastly, we obtain (9) by defining the following two matrice.

References

[1] D. Macdonald, Reflections on the history of electrochemical impedance spectroscopy, Electrochim. Acta 51 (8-9) (2006) 1376–1388.
[2] J. Macdonald, D. Franceschetti, Precision of impedance spectroscopy estimates of bulk, reaction rate, and diffusion parameters, J. Electroanal. Chem. 307 (1-2) (1991) 1–11.
[3] J. Macdonald, Comparison of Parametric and Nonparametric Methods for the Analysis and Inversion of Immittance Data: Critique of Earlier Work, J. Comp. Phys. 157 (1) (2000) 280–301.
[4] F. Ciucci, Y. Hao, D.G. Goodwin, Impedance spectra of mixed conductors: a 2D study of ceria, Phys. Chem. Chem. Phys. 11 (47) (2009) 11243–11257.
[5] F. Ciucci, W.C. Chueh, D.G. Goodwin, S.M. Haile, Surface reaction and transport in mixed conductors with electrochemically-active surfaces: a 2-D numerical study of ceria, Phys. Chem. Chem. Phys. 13 (6) (2011) 2121–2135.
[6] C. Chen, D. Chen, W.C. Chueh, F. Ciucci, Modeling the impedance response of mixed-conducting thin film electrodes, Phys. Chem. Chem. Phys. 16 (2014) 11573–11583.
[7] W. Lai, S. Haile, Impedance spectroscopy as a tool for chemical and electrochemical analysis of mixed conductors: A case study of ceria, J. Am. Cer. Soc. 88 (11) (2005) 2979–2997.
[8] J. Jamnik, J. Maier, Generalised equivalent circuits for mass and charge transport: chemical capacitance and its implications, Phys. Chem. Chem. Phys. 3 (9) (2001) 1668–1678.
[9] J.R. Macdonald, Comparison of Some Random-Barrier, Continuous-Time Random-Walk, and Other Models for the Analysis of Wide-Range Frequency Response of Ion-Conducting Materials, The Journal of Physical Chemistry B 113 (27) (2009) 9175–9182.
[10] J.R. Macdonald, Comments on the electric modulus formalism model and superior alternatives to it for the analysis of the frequency response of ionic conductors, Journal of Physics and Chemistry of Solids 70 (3-4) (2009) 546–554.
[11] J.R. Macdonald, Utility of continuum diffusion models for analyzing mobile-ion immittance data: electrode polarization, bulk, and generationrecombination effects, Journal of Physics: Condensed Matter 22 (49) (2010) 495101.
[12] J.R. Macdonald, Utility and Importance of Poisson-Nernst-Planck Immittance-Spectroscopy Fitting Models, The Journal of Physical Chemistry C 117 (45) (2013) 23433–23450.
[13] J.R. Macdonald, Impedance spectroscopy, Ann. Biomed. Eng. 20 (3) (1992) 289–305.
[14] E. Barsoukov, J. Macdonald (Eds.), Impedance Spectroscopy: Theory, Experiment, and Applications, 2nd Edition, Wiley and Sons, New York, 2005.

[15] M.E. Orazem, B. Tribollet, Electrochemical Impedance Spectroscopy, Wiley Interscience, 2008.
[16] J. Macdonald, W. Thompson, Strongly Heteroscedastic Nonlinear Regression, Commun. Stat. Simulat. 20 (4) (1991) 843–886.
[17] M. Orazem, P. Agarwal, L. Garcia-Rubio, Critical issues associated with interpretation of impedance spectra, J. Electroanal. Chem. 378 (1-2) (1994) 51–62.
[18] Z. Stoynov, D. Vladikova, Differential Impedance Analysis, Marin Drinov Academic Publishing House, 2005.
[19] D. Vladikova, G. Raikova, Z. Stoynov, H. Takenouti, J. Kilner, S. Skinner, Differential impedance analysis of solid oxide materials, Solid State Ionics 176 (25-28) (2005) 2005–2009.
[20] A. Barbucci, M. Viviani, P. Carpanese, D. Vladikova, Z. Stoynov, Impedance analysis of oxygen reduction in SOFC composite electrodes, Electrochim. Acta 51 (8-9) (2006) 1641–1650.
[21] Z. Stoynov, Advanced Impedance Techniques for Lithium Batteries Study, in: C. Julien, Z. Stoynov (Eds.), Materials for Lithium-Ion Batteries, Vol. 85 of NATO Science Series, Springer, Netherlands, 2000, pp. 371–380.
[22] D. Vladikova, Impedance of Lithium Ion Batteries - Basic Models and Differential Analysis, in: C. Julien, Z. Stoynov (Eds.), Materials for Lithium-Ion Batteries, Vol. 85 of NATO Science Series, Springer, Netherlands, 2000, pp. 593–596.
[23] F. Dion, A. Lasia, The use of regularization methods in the deconvolution of underlying distributions in electrochemical processes, J. Electroanal. Chem. 475 (1) (1999) 28–37.
[24] E. Ivers-Tiffée, A. Weber, H. Schichlein, Handbook of Fuel Cells, John Wiley & Sons, Ltd, 2010.
[25] M. Orazem, P. Shukla, M. Membrino, Extension of the measurement model approach for deconvolution of underlying distributions for impedance measurements, Electrochim. Acta 47 (13-14) (2002) 2027–2034.
[26] H. Schichlein, A. Müller, M. Voigts, A. Krügel, E. Ivers-Tiffée, Deconvolution of electrochemical impedance spectra for the identification of electrode reaction mechanisms in solid oxide fuel cells, J. Appl. Electrochem. 32 (8) (2002) 875–882.
[27] B. Liu, H. Muroyama, T. Matsui, K. Tomida, T. Kabata, K. Eguchi, Analysis of Impedance Spectra for Segmented-in-Series Tubular Solid Oxide Fuel Cells, J. Electrochem. Soc. 157 (12) (2010) B1858–B1864.
[28] A. Tesler, D. Lewin, S. Baltianski, Y. Tsur, Analyzing results of impedance spectroscopy using novel evolutionary programming techniques, J. Electroceram. 24 (4) (2010) 245–260.
[29] H. Sumi, T. Yamaguchi, K. Hamamoto, T. Suzuki, Y. Fujishiro, T. Matsui, K. Eguchi, AC impedance characteristics for anode-supported microtubular solid oxide fuel cells, Electrochim. Acta 67 (2012) 159–165.
[30] J. Weese, A reliable and fast method for the solution of Fredhol integral equations of the first kind based on Tikhonov regularization, Comp. Phys. Comm. 69 (1) (1992) 99–111.
[31] R. Renaut, R. Baker, M. Horst, C. Johnson, D. Nasir, Stability and error analysis of the polarization estimation inverse problem for microbial fuel cells, Inverse Problems 29 (4) (2013), 045006 (24pp).
[32] J. Winterhalter, D.G. Ebling, D. Maier, J. Honerkamp, An improved analysis of admittance data for high resistivity materials by a nonlinear regularization method, J. Appl. Phys. 82 (11) (1997) 5488–5495.
[33] J. Winterhalter, D.G. Ebling, D. Maier, J. Honerkamp, Analysis of Admittance Data: Comparison of a Parametric and a Nonparametric Method, J. Comp. Phys. 153 (1) (1999) 139–159.
[34] J. Macutkevic, J. Banys, A. Matulis, Determination of the Distribution of the Relaxation Times from Dielectric Spectra, Nonlinear Anal. Model. Control 9 (1) (2004) 75–88.
[35] A. Mikonis, J. Banys, R. Grigalaitis, A. Matulis, S. Lapinskas, G. Völkel, Determination of the two dimensional distribution of the attempt relaxation times and activation energies from temperature dependence of dielectric dispersion, Cent. Eur. J. Phys. 11 (2) (2013) 206–212.
[36] J. Hansen, J. Hogue, G. Sander, R. Renaut, S. Popat, Non-negatively constrained least squares and parameter choice by the residual periodogram for the inversion of electrochemical impedance spectroscopy, arXiv e-print arXiv:1309.4498.
[37] J. Schmidt, P. Berg, M. Schönleber, A. Weber, E. Ivers-Tiffée, The distribution of relaxation times as basis for generalized time-domain models for Li-ion batteries, J. of Power Sources 221 (2013) 70–77.
[38] E. Tuncer, S. Gubanski, On dielectric data analysis. Using the Monte Carlo method to obtain relaxation time distribution and comparing non-linear spectral function fits, IEEE T. Dielect. El. In. 8 (3) (2001) 310–320.
[39] E. Tuncer, J. Macdonald, Comparison of methods for estimating continuous distributions of relaxation times, J. Appl. Phys. 99 (7) (2006), 074106 (4pp).
[40] T. Hörlin, Deconvolution and maximum entropy in impedance spectroscopy of noninductive systems, Solid State Ionics 107 (3-4) (1998) 241–253.
[41] S. Hershkovitz, S. Baltianski, Y. Tsur, Harnessing evolutionary programming for impedance spectroscopy analysis: A case study of mixed ionic-electronic conductors, Solid State Ionics 188 (1) (2011) 104–107.
[42] S. Hershkovitz, S. Tomer, S. Baltianski, Y. Tsur, ISGP: Impedance Spectroscopy Analysis Using Evolutionary Programming Procedure, ECS Trans. 33 (40) (2011) 67–73.
[43] G. Golub, P. Hansen, D. O'Leary, Tikhonov Regularization and Total Least Squares, SIAM J. Matrix Anal. A. 21 (1) (1999) 185–194.
[44] R. Tibishirani, Regression Shrinkage and Selection via the Lasso, J. R. Statist. Soc. B 58 (1) (1996) 267–288.
[45] O. Christensen, K. Christensen, Approximation Theory: From Taylor Polynomials to Wavelets, Applied and Numerical Harmonic Analysis, Springer, 2005.
[46] L. Trefethen, Approximation Theory and Approximation Practice, Society for Industrial and Applied Mathematics, 2012.
[47] A.R. Davies, N.J. Goulding, Wavelet regularization and the continuous relaxation spectrum, J. Non-newton. Fluid. 189-190 (2012) 19–30.
[48] T. Hastie, R. Tibshirani, J. Friedman, The Elements of Statistical Learning, Springer Series in Statistics, Springer, New York, 2009.
[49] C.L. Mallows, Some Comments on C P, Technometrics 15 (4) (1973) 661–675.
[50] C.R. Vogel, Computational Methods for Inverse Problems, SIAM, 2002.
[51] V.A. Morozov, Methods for Solving Incorrectly Posed Problems, Springer, 1984.
[52] G.H. Golub, M. Heath, G. Wahba, Generalized, Cross-Validation as a Method for Choosing a Good Ridge Parameter, Technometrics 21 (2) (1979) 215–223.
[53] P. Hansen, Analysis of Discrete Ill-Posed Problems by Means of the L-Curve, SIAM Rev. 34 (4) (1992) 561–580.
[54] P. Hansen, D. O'Leary, The Use of the L-curve in the Regularization of Discrete Ill-Posed Problems, SIAM J. Sci. Comput. 14 (6) (1993) 1487–1503.
[55] P.C. Hansen, M.E. Kilmer, R.H. Kjeldsen, Exploiting Residual Information in the Parameter Choice for Discrete Ill-Posed Problems, BIT Numer. Math. 46 (1) (2006) 41–59.
[56] B.W. Rust, D.P. O'Leary, Residual periodograms for choosing regularization parameters for ill-posed problems, Inverse Probl. 24 (3) (2008), 034005 (30pp).
[57] C.R. Vogel, Non-convergence of the L-curve regularization parameter selection method, Inverse Probl. 12 (4) (1996) 535–547.
[58] A.M. Thompson, J.W. Kay, D.M. Titterington, A cautionary note about crossvalidatory choice, J. Stat. Comput. Simul. 33 (4) (1989) 199–216.
[59] J.T. Kent, M. Mohammadzadeh, Global optimization of the generalized cross-validation criterion, Stat. Comput. 10 (3) (2000) 231–236.
[60] T. Hesterberg, N.H. Choi, L. Meier, C. Fraley, Least angle and l_1 penalized regression: A review, Statist. Surv. 2 (2008) 61–93.
[61] S. Arlot, A. Celisse, A survey of cross-validation procedures for model selection, Statist. Surv. 4 (2010) 40–79.
[62] B.A. Boukamp, J. Macdonald, Alternatives to kronig-kramers transformation and testing, and estimation of distributions, Solid State Ionics 74 (1994) 85–101.
[63] A. Sadkowski, CNLS fits and Kramers-Kronig validation of resonant EIS data, J. Electroanal. Chem. 573 (2) (2004) 241–253.
[64] M.E. Orazem, A systematic approach toward error structure identification for impedance spectroscopy, J. Electroanal. Chem. 572 (2) (2004) 317.
[65] S.L. Carson, M.E. Orazem, O.D. Crisalle, L. Garcia-Rubio, On the error structure of impedance measurements: Simulation of psd instrumentation, J. Electrochem. Soc. 150 (10) (2003) E491–E500.
[66] F. Ciucci, T. Carraro, W.C. Chueh, W. Lai, Reducing error and measurement time in impedance spectroscopy using model based optimal experimental design, Electrochim. Acta 56 (15) (2011) 5416–5434.
[67] F. Ciucci, Revisiting parameter identification in electrochemical impedance spectroscopy: Weighted least squares and optimal experimental design, Electrochim. Acta 87 (2013) 532–545.
[68] C. Huang, D. Chen, Y. Lin, R. Ran, Z. Shao, Evaluation of $Ba_{0.6}Sr_{0.4}Co_{0.9}Nb_{0.1}O_{3-\delta}$ mixed conductor as a cathode for intermediate-temperature oxygen-ionic solid-oxide fuel cell, Journal of Power Sources 195 (16) (2010) 5176–5184.
[69] K. Zhang, R. Ran, L. Ge, Z. Shao, W. Jin, N. Xu, Systematic investigation on new $SrCo_{1-y}Nb_yO_{3-\delta}$ ceramic membranes with high oxygen semi-permeability, Journal of Membrane Science 323 (2) (2008) 436–443.
[70] D. Chen, C. Chen, F. Dong, Z. Shao, F. Ciucci, Cobalt-free Polycrystalline $Ba_{0.95}La_{0.05}FeO_{3-\delta}$ Thin Films as Cathodes for Intermediate-Temperature Solid Oxide Fuel Cells, J. of Power Sources 250 (2014) 188–195.
[71] P. Buschel, U. Troltzsch, O. Kanoun, Calculation of the distribution of relaxation times for characterization of the dynamic battery behavior, in: 9th International Multi-Conference on Systems, Signals and Devices (SSD), 2012, pp. 1–3.